

# Data-driven Emergency Frequency Control for Multi-Infeed Hybrid AC-DC System

Qianni Cao, *Student Member, IEEE*, Chen Shen, *Senior Member, IEEE*

**Abstract**—Under frequency load shedding (UFLS) constitutes the very last resort for preventing total blackouts and cascading events. Fluctuating operating conditions and weak resilience of the future grid require UFLS strategies adapt to various operating conditions and non-envisioned faults. This paper develops a novel data-enabled predictive control algorithm KLS to achieve the optimal one-shot load shedding for power system frequency safety. The algorithm utilizes a latent extractor network to track parameter variations in the system dynamic model, enabling a coordinate transformation from the delay embedded space to a new space where the dynamics can be linearly represented. To address approximation inaccuracies and the discrete nature of load shedding, a safety margin tuning scheme is integrated into the KLS framework, ensuring that the system frequency trajectory remains within the safety range. Simulation results show the adaptability, prediction capability and control effect of the proposed UFLS strategy.

**Index Terms**—Koopman theory, UFLS, time delays, optimal emergency frequency control, parameter uncertainty.

## NOMENCLATURE

### Indices

## I. INTRODUCTION

### A. Motivation

**U**NDER frequency events in bulk power systems are generally caused by sudden large active power deficits, such as generator tripping or load surges. Restraining such frequency unsafety is essential for the secure operation of power systems.

Under frequency load shedding (UFLS) constitutes the very last resort for preventing total blackouts and cascading events. The most standard and widely used strategy is to shed pre-assigned loads in discrete steps or blocks; each stage is implemented when the frequency is lower than a preset level of load shedding. In modern power systems, the uncertainty of renewable generation lead to ever-fluctuating operating conditions. The conventional UFLS strategy, which determines the load shedding amount based on anticipated operating conditions and faults, faces challenges in effectively working well under various operating conditions [1]. Therefore, it is necessary to develop UFLS schemes that adapt to various operating conditions and events, decide the optimal load shedding amount to promise the hard limits on the frequency trajectories.

In this paper, an online data-enabled UFLS scheme is designed for emergency frequency control. With the frequency prediction capability under various operating conditions and power imbalances, it leverages online input/output measurements to achieves safe and optimal online control with minimal

one-shot load shedding, instead of shedding loads at multi stages, thereby speeding up the recovery of system frequency.

### B. Literature Review

There have been abundant works on frequency control. A challenging problem is optimal frequency trajectory tracking, where a control policy should drive a dynamical system within safety range while minimizing load shedding amount. A general solution is to formulate control problems as optimization problems. The key ingredient for optimal control problem is an accurate parametric state space model of the system.

A standard solution is utilizing classical representations of system dynamics, such as the swing equation and the first-order PFR dynamics. These methods require prior knowledge of system parameters [2], [2]–[4], or the need to know the power deficit in the system when faults occur [5]. However, parameters such as inertia have become difficult to obtain accurately due to the high penetration of power electronics converter-interfaced devices [6]. Moreover, the power deficit in the system cannot be measured directly in practical power networks. Although some methods such as [7] use data-driven approaches to estimate these parameters, the accuracy of the model itself may be limited. For example, the traditional SFR model does not explicitly consider the impact of load-frequency dependence [8].

As power systems are becoming more complex and data is becoming more readily available, it is necessary to develop methods that uses only input/output data measured from the unknown system to predict the future trajectories [9]. Since nonlinear system dynamics renders the optimal control problem intractable, it is desirable that the learned system model linear. Koopman-based control framework [10] was proposed to provide linear representations of system dynamics in the context of black-box systems.

Fluctuating operating conditions and weak resilience of the future grid require frequency control strategies adapt to various operating conditions and non-envisioned faults. Achieving generalization capability is one of the key challenges in data-driven control. Otherwise, for anticipated operating conditions and faults, control strategies can be devised through offline pre-decision making and online matching, thereby diminishing the significance of data-driven control. However, there is no guarantee that a system model trained for specific predetermined scenarios generalize to data outside of the distribution of the training set [11]–[13]. Hence, it is of utmost importance to enhance the generalization capability of data-driven control. The extraction of model parameter information from the training set, obtained under predetermined operating

conditions and envisioned fault scenarios, is critical. For data-driven control based on the identified system, the generalization capability relies on the prediction capability of the identified system. In other words, Koopman linear representations should be able to track parameter variations in the original parametric state space system model using measurements.

Since Koopman operator is infinite-dimensional, finite Koopman invariant subspace is often approximated to gear toward prediction and control. However, representation errors of Koopman operators are inevitable [14], [15]. Inaccurate estimations and predictions may degrade the quality of the obtained optimal control. In Ref. [16], the impact of representation errors of Koopman eigenpairs on the control performance of LQR controllers was evaluated. The adaptive nature of closed-loop control theoretically allows one to compensate for modeling discrepancies and to account for disturbances [14]. However, in practice, the control decision-making in power systems relies on simulation models. To mitigate the risks associated with inaccurate simulation model parameters and algorithm limitations, closed-loop strategies involving load shedding measures are rarely implemented [17]. Therefore, it is necessary to address the potential impact of representation errors on open-loop control.

Moreover, in most load shedding schemes, it is often assumed that the load shedding amount at each bus can be a continuous value [12], [18]. This assumption overlooks the fact that load shedding is accomplished by shedding candidate feeders. In practical engineering, the feasible amount of load shedding is restricted to discrete values, with each discrete interval representing the load associated with a feeder. Although the optimal control problem can be formulated as an MILP problem to decide whether to shed a feeder or not [19], solving MILP is an NP-hard problem, making it difficult for online control. Therefore, Ref. [20]–[22] decides the control inputs at a stage beforehand and then rounds it to the nearest discrete value. However, this leads to a discrepancy between the actual and optimal shedding amounts, which affects the dynamic behavior of the system after control. Consequently, when designing the control policy, it is essential to explicitly consider the potential effects of the discrepancy and ensure that the dynamical system remains within the safety range while minimizing the economic losses caused by load shedding.

### C. Contribution

According to the literature review, to address the frequency stability issue in hybrid AC/DC power grids with high penetration of renewable energy sources, we face three main challenges: 1) system identification for optimal control under unanticipated operating conditions and power imbalance; 2) analyzing the system performance when applying control policies computed from an inaccurate Koopman representations; 3) designing a control strategy that works with discrete feasible load shedding values.

In response to the aforementioned research gaps, the main contributions of this study are outlined as follows:

- 1) We introduces a novel data-enabled predictive control algorithm, referred to as KLS, that achieves optimal

one-shot load shedding for power system frequency safety. The KLS algorithm demonstrates adaptability to diverse operating conditions and under frequency events, allowing for precise load shedding strategies.

- 2) We investigate how approximation inaccuracies in the Koopman linear representations influence the control strategies and controlled frequency trajectories.
- 3) By formulating a safety margin tuning scheme within the framework of KLS, we ensure that the system frequency trajectory remains within the prescribed hard limits when approximation inaccuracies exist and when the feasible amount of load shedding is restricted to discrete values.

The rest of this paper is organized as follows. Section II proposes the KLS strategy for under frequency events. Section III investigates how approximation inaccuracies in the Koopman linear representations influence the control effect and a safety margin tuning method is proposed. In Section IV, an CIGRE-LF system case is presented and the effectiveness of the proposed control strategy is verified. Section V provides the conclusion.

## II. EMERGENCY FREQUENCY CONTROLLER DESIGN

In this section, we design a deep autoencoder network to learn a coordinate transformation from the delay embedded measurement space into a new space where it is possible to represent the dynamics linearly.

Let an autonomous nonlinear dynamical system be governed by

$$\mathbf{x}_{t+1} = \mathbf{f}(\mathbf{x}_t, \mathbf{y}_t) \quad (1)$$

where  $t = 1, 2, \dots, T$ ,  $T$  is the prediction horizon,  $\mathbf{x} \in R^{n_x}$  is the state,  $\mathbf{y} \in R^{n_y}$  denotes algebraic variables and  $\mathbf{f}(\cdot)$  is a nonlinear function. Considering the computational inefficiency of calculating optimal control for high-dimensional nonlinear dynamical functions, Koopman theory [23] provides a perspective that nonlinear dynamics can be represented in terms of an infinite-dimensional linear operator acting on the space of all possible measurement functions of the system. Even if the function  $\mathbf{f}(\cdot)$  is unknown, it is still possible to estimate the Koopman operator using the system's measurements.

However, the estimation of the Koopman operator relies exclusively on data, either numerical or experimental. In the context of power systems, it is common practice to rely on numerical data acquired from simulations. When collecting the dataset, it is necessary to preset the operation conditions and emergency events to trigger the system dynamics. Diverse operational conditions lead to variations in the parameters of the grid state space model given in Eq.(1), and also, the Koopman linear representations [14]. Thus, a significant challenge in linear predictive system modeling is adaption to different operating conditions and faults in the training set.

Although it is feasible to incorporate a wide range of operation conditions and events within the training set, it is impractical to exhaustively account for every scenario. Therefore, the linear representation should also possess the ability to generalize, allowing the linear dynamic model of the system, which is trained for specific predetermined scenarios, to extend its prediction capability to systems operating under

non-predefined conditions and faults that are not included in the sample set.

In order to explicitly represent the variations of operating conditions and the complexity of emergency events in the state space grid model Eq. (1), we utilize a vector of variables  $\mathbf{m}$  to represent a subset of uncertain model parameters that are challenging to obtain online. To incorporate the uncertainty of these parameters into the system model, a modified model is evaluated as

$$\begin{aligned} \mathbf{x}_{t+1} &= \mathbf{f}(\mathbf{x}_t, \mathbf{y}_t, \mathbf{m}_t) \\ \mathbf{m}_{t+1} &= \mathbf{h}(\mathbf{x}_t, \mathbf{y}_t, \mathbf{m}_t) \end{aligned} \quad (2)$$

Compared with Eq.(1), Eq.(2) provides a more general form of a deterministic power system model which accounts for uncertainties. In Eq.(2),  $\mathbf{x}_a^\top = [\mathbf{x}^\top \ \mathbf{m}^\top]$  can be defined as pseudo-state variables. The augmented model was first introduced in Ref. [24].

**Remark 1:** Many model parameters are typically assumed to be time-invariant, although their initial values may vary across different data samples, such as system inertia. Additionally, there exist time-varying parameters, but their temporal variations can be captured using discrete-time dynamic equations, as presented in Eq. (2), for instance, the power deficit in the system.

Since  $\mathbf{m}$  are hard to measure, which constitutes hidden, or latent variables that are not directly measured but are dynamically important. Thus, the challenge of adapting the linear representations to accommodate the parameters variations transforms into the challenge of accounting for the hidden variable in the model.

Time-delay embedding provides an approach to augment these hidden variables, and under certain conditions, given by Takens' embedding theorem [25], the delay-augmented state yields an attractor that is diffeomorphic (i.e. continuously differentiable deformable) to the underlying, though unmeasured, full-state attractor. Here, we design a custom deep autoencoder network to learn a coordinate transformation from the delay embedded space into a new space where it is possible to represent the dynamics in a linear form and also to track the parameter variations in the system with input/output data.

The custom deep auto encoder networks is illustrated as follows.

The data set collected for training the deep auto encoder networks is described as follows. For a given power system, a specific anticipated operating condition  $\alpha \in \mathcal{A}$  is considered, and a representative fault  $\beta \in \mathcal{B}$  is introduced.  $\mathcal{A}$  represents a predefined set of typical operating conditions.  $\mathcal{B}$  denotes a predefined set of typical faults. Additionally, load shedding amount  $\mathbf{u} = [u_1, \dots, u_i, \dots, u_I] \in \mathcal{U}$  are defined at each load node  $i$ , where  $u_i (i = 1, 2, \dots, I)$  (in per unit, where the load level at bus  $i$  is the base value for  $u_i$ ) is a uniformly distributed random number between 0 and 1. Subsequently, time-series data of the system's inertia center frequency (referred to as the system frequency hereafter)  $\Omega = \{\omega^{\alpha, \beta} | \alpha \in \mathcal{A}, \beta \in \mathcal{B}\}$  are collected at time points  $t = 1, 2, \dots, T$ , resulting in a sequence of data  $[\omega_1^{\alpha, \beta}, \omega_2^{\alpha, \beta}, \dots, \omega_T^{\alpha, \beta}]$ . The obtained  $\Omega$  and  $\mathbf{u} \in \mathcal{U}$  are utilized as training data for the linear prediction model. Details

for the network architecture and training are given in Appendix A.

Based on Koopman theory, we assuming that the frequency dynamics of the system is governed by the linear dynamic system equation represented in Eq.(3).

$$\mathbf{g}_{t+1} = \mathbf{A}\mathbf{g}_t + \mathbf{B}\mathbf{u}_t \quad (3)$$

where

$$\mathbf{g}_t = \begin{bmatrix} \omega_t \\ \varphi(\omega_{t-\tau:t}, \mathbf{y}_{t-\tau:t}) \end{bmatrix} \quad (4)$$

where  $\omega_t$  is the deviation of frequency from its nominal value (in per unit) at time  $t$ ,  $\omega_{t-\tau:t} = [\omega_{t-\tau}, \omega_{t-\tau+\Delta t}, \dots, \omega_t]$ ,  $\mathbf{y}_{t-\tau:t} = [y_{t-\tau}, y_{t-\tau+\Delta t}, \dots, y_t]$  represent the time series of system frequency (state variable) and voltages (algebraic variables), respectively.  $\varphi$  denotes a neural network with a prescribed activation function and connectivity structure. With methodology provided in Appendix A, it is feasible to train the parameters of  $\varphi$ , as well as the matrices  $\mathbf{A}$  and  $\mathbf{B}$ .

With the known parameters of  $\varphi$ ,  $\mathbf{A}$ , and  $\mathbf{B}$ , one can utilize Eq. (3) to predict the future trajectory of the system frequency variation given  $\omega_1^{\alpha, \beta}$  and  $\mathbf{u}$ . Herein, we refer to the dynamical system described by Equation (3) as a Koopman linear system. Given the inevitable presence of training errors in the parameters of  $\varphi$ ,  $\mathbf{A}$ , and  $\mathbf{B}$ , the frequency trajectory of the Koopman linear system may deviate from the actual trajectory. For the purposes of clarity, we denote the former as  $[\bar{\omega}_2^{\alpha, \beta}, \dots, \bar{\omega}_T^{\alpha, \beta}]$ .

**Remark 1:** The time intervals in the time points  $t = 1, 2, \dots, T$  may not be consistent with the time intervals in  $t - \tau, t - \tau + \Delta t, \dots, t$ . In Section IV, the time intervals in  $t = 1, 2, \dots, T$  are set to 1 s, while in  $t - \tau, t - \tau + \Delta t, \dots, t$ ,  $\Delta t$  is set to 1 ms.

#### A. Koopman-Operator-Based Emergency Frequency Control Strategy

Combined with the Koopman model predictive control proposed in Ref. [26], the optimal shedding amount is obtained by solving the following optimal control problem.

$$\begin{aligned} \min \quad & \mathbf{u}^\top \mathbf{R} \mathbf{u} \\ \text{s.t.} \quad & \bar{\omega}_t \geq \omega_{\min}, \quad \forall t \in T \\ & \bar{\omega}_T \geq \omega_{\infty \min} \\ & \mathbf{g}_{t+1} = \mathbf{A}\mathbf{g}_t + \mathbf{B}\mathbf{u}_t, \quad \forall t \in T \end{aligned} \quad (5)$$

where  $\mathbf{R}$  represents a positive definite matrix used to represent the cost of load shedding at each bus,  $\bar{\omega}_t$  system frequency at time  $t$  predicted by Koopman linear system,  $\omega_{\min}$  is the maximum allowed frequency deviation,  $\omega_{\infty \min}$  is the maximum allowed steady-state frequency deviation. The optimal control problem Eq.(5) is a quadratic programming problem with  $\mathbf{R}$  being a positive definite matrix. This problem can be solved in polynomial time.

**Remark 1:** The values of  $\omega_{\min}$  and  $\omega_{\infty \min}$  can be adjusted based on the interplay between data-driven load shedding and the traditional UFLS scheme. The traditional UFLS scheme,

as it initiates load shedding after a certain deviation in system frequency occurs (e.g., when the system frequency drops to 49Hz), may lead to larger system faults due to the delayed timing of load shedding, resulting in greater power deficits and consequently higher load losses. If the objective of data-driven load shedding is to avoid triggering the traditional UFLS scheme,  $\omega_{\min}$  can be set to 49.0Hz. On the other hand, if the data-driven load shedding aims to fully replace the traditional UFLS scheme and ensure that the system's minimum frequency remains above the minimum operating frequency of synchronous generators (e.g., 47Hz),  $\omega_{\min}$  can be set to -3Hz. In Section IV, we choose  $\omega_{\min}$  as 49.0Hz as an illustrative example to show the effectiveness of KLS control.

In practice, continuous adjustment of load shedding is difficult to achieve, and it is often necessary to choose whether or not to shed a load on a particular feeder line, resulting in a series of discrete values for the actual load shedding. Let the optimal load shedding obtained by solving the optimal control problem Eq.(5) be denoted as  $\bar{\mathbf{u}}_* = [\bar{u}_{1*}, \dots, \bar{u}_{i*}, \dots, \bar{u}_{I*}]$  the actual load shedding amount would then be given as

$$Q_d(\bar{u}_{i*}) = \begin{cases} nd & nd \leq \bar{u}_{i*} < n(d+0.5) \\ n(d+1) & n(d+0.5) \leq \bar{u}_{i*} < n(d+1) \end{cases} \quad (6)$$

where  $d$  represents the quantization interval, which physically refers to the load shedding amount on a single feeder line,  $n$  represents a positive integer, and  $Q_d(\bar{u}_{i*})$  denotes the actual load shedding amount at each load node  $i$  when the discrete interval is  $d$ . Solving the optimal control problem in Eq. (5) and rounding the resulting solution as described in Eq. (6) is referred to as Koopman-based load shedding strategy (KLS).

**Remark 1:** After obtaining the optimal load shedding amount solving the optimization problem Eq. (5), instead of rounding it to the nearest feasible value, as given in Eq. (6), an alternative approach is to round the computed control quantity to the nearest larger value, as outlined below.

$$Q_d(\bar{u}_{i*}) = n(d+1) \quad nd < \bar{u}_{i*} \leq n(d+1) \quad (7)$$

However, the strategy in Eq.(7) results in over-shedding. Although, given the same system linear representation, the strategy presented in Eq.(7) with a larger load shedding amount compared to Eq.(6) is more likely to ensure that the system frequency does not violate safety constraints. Nevertheless, when implementing the strategy described in Eq.(6), it is also possible to ensure the safety of the system frequency by tuning a safety margin in the constraints of Eq.(5). The design of the safety margin in KLS will be presented in Section III-B. By avoiding the rounding of the optimal load shedding amount to the nearest larger value, we achieve a smaller amount of load shedding while maintaining system frequency safety (this will be demonstrated in Section IV).

### III. ERROR ESTIMATION AND SAFETY MARGIN DESIGN

#### A. Impact of Koopman representation errors on control effects

In Section II, we employed constraints in the optimal control problem to ensure that the frequency nadir and steady-state frequency in the Koopman prediction model remain above the acceptable minimum values. However, in actual power systems,

there is a possibility that the optimal load shedding obtained from Eq. (5) may prove ineffective when applied. This means that in the real system, the frequency trajectory may violate the prescribed hard limits. Therefore, in this section, we first analyze some of the main reasons for the failure of the optimal strategy obtained from Eq. (5). Secondly, we propose adding a safety margin to the frequency limits in constraints of Eq. (5). An explicit approach is introduced for calculating the safety margin. By integrating the safety margin, the optimal control strategy derived from KLS effectively ensures that the system frequency complies with the prescribed hard limits in the actual system.

Despite attempts to develop the accurate system dynamics, there are inevitable representation errors of the finite-dimensional approximation of the Koopman operator, manifesting as minor prediction errors. In the actual system, assuming the existence of an optimal load shedding amount that ensures the system frequency adheres strictly to predefined hard limits while minimizing the load shedding amount, we refer to the load shedding amount as the actual optimal control strategy. In the presence of deviations between the obtained and actual Koopman linear dynamics, it is crucial to investigate how the disparities between the optimal control strategy derived from Eq. (5) and the actual optimal load shedding amount evolve with varying magnitudes of deviation. This analysis aims to determine whether even slight deviations between the obtained and actual Koopman linear dynamics can compromise the desired system properties, potentially violating the imposed hard limits.

Assume that  $\bar{\mathbf{g}}$  and  $(\bar{\mathbf{A}}(x_t), \bar{\mathbf{B}}(x_t))$  can be identified from data, and that the model errors are bounded in terms of the infinity induced norm as

$$\|\Delta_{\mathbf{A}}\| \leq \varepsilon_{\mathbf{A}}, \|\Delta_{\mathbf{B}}\| \leq \varepsilon_{\mathbf{B}}, \forall k \geq 0 \quad (8)$$

where  $\|\Delta_{\mathbf{A}}\| = \|\bar{\mathbf{A}} - \mathbf{A}\|$ ,  $\|\Delta_{\mathbf{B}}\| = \|\bar{\mathbf{B}} - \mathbf{B}\|$ . By applying the definition of  $(\bar{\mathbf{A}}, \bar{\mathbf{B}})$ , modelled system dynamics can be transformed into  $\mathbf{g}$  coordinates:

$$\mathbf{g}_{t+1} = \bar{\mathbf{A}}\mathbf{g}_t + \bar{\mathbf{B}}\mathbf{u}_t + \beta(\mathbf{x}_k) + \varepsilon_{\mathbf{g}}(\bar{\mathbf{A}}\mathbf{g}(x_t) - \mathbf{g}(x_{t+1})) \quad (9)$$

Define  $\gamma(\mathbf{x}_{k+1}) = \beta(\mathbf{x}_k) + \varepsilon_{\mathbf{g}}(\bar{\mathbf{A}}\mathbf{g}(x_t) - \mathbf{g}(x_{t+1}))$ . Further, we assume the disturbance is norm-bounded by:

$$\gamma(\mathbf{x}_k) = \{\gamma \in \mathbb{R}^n \mid \|\gamma\| \leq \varepsilon_{\gamma}\} \quad (10)$$

Define

$$\mathcal{R} = \begin{bmatrix} \mathbf{R}_{0,0} & & & \\ \mathbf{R}_{1,1} & \mathbf{R}_{1,0} & & \\ \vdots & \ddots & \ddots & \\ \mathbf{R}_{T,T} & \cdots & \mathbf{R}_{T,1} & \mathbf{R}_{T,0} \end{bmatrix} \quad (11)$$

where  $\mathbf{R}_{i,j}$  is a matrix of compatible dimension. We denote the set of such matrices by  $\mathcal{L}^{T,p \times q}$ .  $\mathcal{R}$  denoted the  $i$ -th block column of  $\mathbf{R}$ , both indexing from 0. For dynamics in Eq.(2) and a fixed horizon  $T$ , we define  $\mathbf{x}$  and  $\mathbf{u}$  as the stacked states  $\mathbf{x}_{0:T}$ , and inputs  $\mathbf{u}_{0:T}$ , up to time  $T$ , i.e.,

$$\mathbf{F}^{\top}(\mathbf{x}) = [\mathbf{g}^{\top}(\mathbf{x}_0) \quad \mathbf{g}^{\top}(\mathbf{x}_1) \quad \cdots \quad \mathbf{g}^{\top}(\mathbf{x}_T)] \quad (12)$$

$$\mathbf{u}^\top = [\mathbf{u}_0^\top \quad \mathbf{u}_1^\top \quad \cdots \quad \mathbf{u}_T^\top] \quad (13)$$

$$\gamma^\top = [x_0^\top \quad \gamma_0^\top \quad \cdots \quad \gamma_{T-1}^\top] \quad (14)$$

where  $\mathbf{u}_0 = \mathbf{u}_1 = \cdots = \mathbf{u}_T$  for one-shot load-shedding.

We can concatenate the dynamics matrices as  $\mathcal{A} = \text{blkdiag}(\mathbf{A}, \cdots, \mathbf{A}, 0)$ ,  $\mathcal{B} = \text{blkdiag}(\mathbf{B}, \cdots, \mathbf{B}, 0)$ . Note that we embed  $x_0$  as the first component of the disturbance process. Based on System Level Synthesis (SLS) [27], [28], we have a direct optimization over system responses  $\phi_g, \phi_u$  defined as

$$\begin{bmatrix} F^\top(\mathbf{x}) \\ \mathbf{u}_* \end{bmatrix} = \begin{bmatrix} \phi_g \\ \phi_u \end{bmatrix} \gamma \quad (15)$$

where  $\phi_g \in \mathcal{L}^{T, n \times n}$ ,  $\phi_u \in \mathcal{L}^{T, m \times n}$  are two block-lower triangular matrices.

It has been proved that for any  $\{\phi_g, \phi_u\} \in \mathcal{L}$  satisfying

$$[\mathbb{I} - Z\mathcal{A} \quad -Z\mathcal{B}] \begin{bmatrix} \phi_g \\ \phi_u \end{bmatrix} = \mathbb{I} \quad (16)$$

the controller  $\phi_u \phi_g^{-1} \in \mathcal{L}$  achieves the desired response, where  $Z$  is the block-downshift operator, i.e., a matrix with the identity matrix on the first block subdiagonal and zeros elsewhere.

For the identified model  $\bar{\mathcal{A}} = \text{blkdiag}(\bar{\mathbf{A}}, \cdots, \bar{\mathbf{A}}, 0)$  and  $\bar{\mathcal{B}} = \text{blkdiag}(\bar{\mathbf{B}}, \cdots, \bar{\mathbf{B}}, 0)$ , the block-lower triangular matrices  $\{\bar{\phi}_g, \bar{\phi}_u\}$  satisfying:

$$[\mathbb{I} - Z\bar{\mathcal{A}} \quad -Z\bar{\mathcal{B}}] \begin{bmatrix} \bar{\phi}_g \\ \bar{\phi}_u \end{bmatrix} = \mathbb{I} \quad (17)$$

By rewriting Eq.(17), we can obtain

$$[\mathbb{I} - Z\mathcal{A} \quad -Z\mathcal{B}]\bar{\phi} = \mathbb{I} - Z\Delta\bar{\phi} \quad (18)$$

where  $\Delta = Z[\Delta_{\mathcal{A}} \quad \Delta_{\mathcal{B}}]$ ,  $\bar{\phi}^\top = [\bar{\phi}_g^\top \quad \bar{\phi}_u^\top]$  and  $\Delta_{\mathcal{A}}, \Delta_{\mathcal{B}}$  are block diagonal matrices satisfying  $\Delta_{\mathcal{A}} = \bar{\mathbf{A}} - \mathbf{A}$ ,  $\Delta_{\mathcal{B}} = \bar{\mathbf{B}} - \mathbf{B}$ . The response of the system  $(\mathcal{A}, \mathcal{B})$  with the controller  $\bar{\phi}_u \bar{\phi}_g^{-1}$  is given by

$$\begin{bmatrix} F^\top(\mathbf{x}) \\ \mathbf{u} \end{bmatrix} = (\bar{\phi} + \bar{\phi}\Delta(\mathbb{I} - \bar{\phi}\Delta)^{-1}\bar{\phi})\gamma \quad (19)$$

We decompose  $\bar{\phi}$ ,  $\Delta$ , and  $\gamma$  as follows to separate the effects of the known initial condition  $x_0$  from the unknown future disturbances  $\gamma_{0:T-1}$ :

$$\bar{\phi} = \begin{bmatrix} \bar{\phi}_g \\ \bar{\phi}_u \end{bmatrix} = \begin{bmatrix} \bar{\phi}^0 & | & \bar{\phi}^{\tilde{\gamma}} \end{bmatrix} \quad (20)$$

$$\gamma = \begin{bmatrix} x_0 \\ \tilde{\gamma} \end{bmatrix}, \Delta = \begin{bmatrix} \Delta^0 \\ \Delta^{\tilde{\gamma}} \end{bmatrix} \quad (21)$$

where  $\bar{\phi}^0$  is the first block column of  $\bar{\phi}$ ,  $\Delta^0$  is the first block row of  $\Delta$ . Then we have

$$\begin{bmatrix} \bar{F}(\mathbf{x}) \\ \bar{\mathbf{u}}_* \end{bmatrix} - \begin{bmatrix} F(\mathbf{x}) \\ \mathbf{u}_* \end{bmatrix} = (\bar{\phi} - \phi)\gamma + \bar{\phi}^{\tilde{\gamma}}\Delta^{\tilde{\gamma}}(\mathbb{I} - \bar{\phi}^{\tilde{\gamma}}\Delta^{\tilde{\gamma}})^{-1}\bar{\phi}^{\tilde{\gamma}}\gamma \quad (22)$$

where

$$[\mathbb{I} - Z\mathcal{A} \quad -Z\mathcal{B}](\bar{\phi} - \phi) = \Delta\bar{\phi} = \bar{\phi}^{\tilde{\gamma}}\Delta^{\tilde{\gamma}} \quad (23)$$

and

$$(\mathbb{I} - \bar{\phi}^{\tilde{\gamma}}\Delta^{\tilde{\gamma}})^{-1} = \sum_{k=0}^{\infty} (\bar{\phi}^{\tilde{\gamma}}\Delta^{\tilde{\gamma}})^k \quad (24)$$

where  $\Delta^{\tilde{\gamma}} \leq \varepsilon_{\mathcal{A}} + \varepsilon_{\mathcal{B}}$ . Therefore, it can be concluded that when  $\varepsilon_{\mathcal{A}}$  and  $\varepsilon_{\mathcal{B}}$  converge to 0,  $\|[\bar{F}^\top(\mathbf{x}) \quad \bar{\mathbf{u}}_*^\top]^\top - [F^\top(\mathbf{x}) \quad \mathbf{u}_*^\top]^\top\|$  converges to 0. In other words, the error of the open-loop dynamics is limited by the representation errors of Koopman eigenpairs.

## B. Safety margin tuning

Despite the minor discrepancy between the optimal control strategy derived from Equation (5) and the true optimal load shedding quantity, the subsequent rounding to the nearest feasible value can yield divergent feasible values, resulting in a discrepancy denoted as  $d$ , representing the quantization interval. Even though there is only a small error between the optimal control strategy obtained from Eq. (5) and the actual optimal amount of load shedding, but after rounded to the nearest feasible value, they may be rounded to different feasible values, which causes a discrepancy of  $d$ , which is the quantization interval. Consequently, it's important to revise the optimal control strategy in Eq.(5) to ensure that the system frequency trajectory remains within the prescribed hard limits. In this section, we further design the constraints in Eq. (5) to prevent the rounded optimal control strategy from causing the system frequency to exceed the prescribed hard limits.

**Proposition 1.** By replacing the frequency limits in Eq. (5) with Eq. (25), it ensures that the optimal control strategy obtained from KLS, when rounded to the nearest value, does not violate the prescribed hard limits on the system frequency.

$$\bar{\omega}_t \geq \omega_{\min} + \zeta \quad (25)$$

where  $\zeta$  satisfies

$$\zeta \geq \left\| \mathbf{C} \sum_{k=0}^{t-1} \mathbf{A}^{(t-1)-k} \mathbf{B} \right\| \frac{d}{2} + \max_{\alpha \in \mathcal{A}, \beta \in \mathcal{B}, \mathbf{u} \in \mathcal{U}} \left\| \bar{\omega}_t^{\alpha, \beta}(\mathbf{u}) - \omega_t^{\alpha, \beta}(\mathbf{u}) \right\| \quad (26)$$

where  $\mathbf{C}$  is an observation matrix with the first element equal to 1 and the remaining elements equal to 0.

*Proof.*

$$\begin{aligned} & \left\| \bar{\omega}_t^{\alpha, \beta}(\bar{\mathbf{u}}_*^{\alpha, \beta}) - \omega_t^{\alpha, \beta}(Q_d(\bar{\mathbf{u}}_*^{\alpha, \beta})) \right\| \\ & \leq \left\| \bar{\omega}_t^{\alpha, \beta}(\bar{\mathbf{u}}_*^{\alpha, \beta}) - \bar{\omega}_t^{\alpha, \beta}(Q_d(\bar{\mathbf{u}}_*^{\alpha, \beta})) \right\| \\ & \quad + \left\| \bar{\omega}_t^{\alpha, \beta}(Q_d(\bar{\mathbf{u}}_*^{\alpha, \beta})) - \omega_t^{\alpha, \beta}(Q_d(\bar{\mathbf{u}}_*^{\alpha, \beta})) \right\| \\ & \leq \left\| \mathbf{C} \sum_{k=0}^{t-1} \mathbf{A}^{(t-1)-k} \mathbf{B} \right\| \frac{d}{2} \\ & \quad + \left\| \bar{\omega}_t^{\alpha, \beta}(Q_d(\bar{\mathbf{u}}_*^{\alpha, \beta})) - \omega_t^{\alpha, \beta}(Q_d(\bar{\mathbf{u}}_*^{\alpha, \beta})) \right\| \end{aligned} \quad (27)$$

where  $\bar{\mathbf{u}}_*^{\alpha,\beta}$  represents the optimal load shedding solution obtained by solving Eq. (5), while  $Q_d(\bar{\mathbf{u}}_*^{\alpha,\beta})$  denotes the actual load shedding amounts at each load node  $i$ ,  $\bar{\omega}_t^{\alpha,\beta}(\bar{\mathbf{u}}_*^{\alpha,\beta})$  corresponds to the predicted frequency of the linear prediction system at time  $t$  when the load shedding amount is  $\bar{\mathbf{u}}_*^{\alpha,\beta}$ .  $\omega_t^{\alpha,\beta}(Q_d(\bar{\mathbf{u}}_*^{\alpha,\beta}))$ , and  $\bar{\omega}_t^{\alpha,\beta}(Q_d(\bar{\mathbf{u}}_*^{\alpha,\beta}))$  respectively represent the actual and predicted system frequency at time  $t$  when the load shedding amount is  $Q_d(\bar{\mathbf{u}}_*^{\alpha,\beta})$ . The values of  $\omega_t^{\alpha,\beta}(\cdot)$  can be obtained through power system simulation, while the values of  $\bar{\omega}_t^{\alpha,\beta}(\cdot)$  can be calculated using the linear prediction system Eq.(3).

The proof for the second inequality in Eq.(28) is as follows.

$$\begin{aligned} \bar{\omega}_t(\bar{\mathbf{u}}) - \bar{\omega}_t(Q(\bar{\mathbf{u}})) &= \mathbf{C}\bar{\mathbf{A}}^t \mathbf{g}(\mathbf{x}_0) + \mathbf{C} \sum_{k=0}^{t-1} \bar{\mathbf{A}}^{(t-1)-k} \bar{\mathbf{B}} \mathbf{u}_t \\ &\quad - \mathbf{C}\bar{\mathbf{A}}^t \mathbf{g}(\mathbf{x}_0) - \mathbf{C} \sum_{k=0}^{t-1} \bar{\mathbf{A}}^{(t-1)-k} \bar{\mathbf{B}} Q(\mathbf{u}_t) \\ &= \mathbf{C} \sum_{k=0}^{t-1} \bar{\mathbf{A}}^{(t-1)-k} \bar{\mathbf{B}} (\mathbf{u}_t - Q(\mathbf{u}_t)) \\ &\leq \left\| \mathbf{C} \sum_{k=0}^{t-1} \bar{\mathbf{A}}^{(t-1)-k} \bar{\mathbf{B}} \right\| \frac{d}{2} \end{aligned} \quad (28)$$

The constraints in the optimal control problem Eq. (5) guarantee that the minimum value of  $\bar{\omega}_t^{\alpha,\beta}(\bar{\mathbf{u}}_*^{\alpha,\beta})$  is no less than  $\omega_{\min} + \varsigma$ , and the steady-state value is no less than  $\omega_{\infty \min} + \varsigma$ . Therefore, when the inequality Eq. (25) holds, it ensures that the frequency trajectory of the actual system is within the safety range, under the load shedding amount  $Q_d(\bar{\mathbf{u}}_*^{\alpha,\beta})$ . ■

$$\begin{aligned} \zeta &= \left\| \mathbf{C} \sum_{k=0}^{t-1} \bar{\mathbf{A}}^{(t-1)-k} \bar{\mathbf{B}} \right\| \frac{d}{2} \\ &\quad + \max_{\alpha,\beta} \left\| \bar{\omega}_t^{\alpha,\beta}(Q_d(\bar{\mathbf{u}}_*^{\alpha,\beta})) - \omega_t^{\alpha,\beta}(Q_d(\bar{\mathbf{u}}_*^{\alpha,\beta})) \right\| \end{aligned} \quad (29)$$

**Remark 1:** Comparing Eq.(25) and Eq.(28), the maximum frequency prediction error of the Koopman linear system on the training and testing sets is employed as an estimate of  $\left\| \bar{\omega}_t^{\alpha,\beta}(Q_d(\bar{\mathbf{u}}_*^{\alpha,\beta})) - \omega_t^{\alpha,\beta}(Q_d(\bar{\mathbf{u}}_*^{\alpha,\beta})) \right\|$ . This estimation is valid when there is an insignificant correlation between the frequency prediction error of the Koopman linear system and  $d$ . Given that  $u_i$  follows a uniform distribution in the training set, we deduce the presence of this circumstance.

**Remark 2:** Although manual tuning of  $\zeta$  is possible, for instance, by calculating the system frequency after rounding the optimal control strategy to the nearest value for each operational condition and fault in the training set and selecting samples where the system frequency fails to meet the hard limits, **Proposition 1** offers an analytical approach for tuning of  $\zeta$ . This approach eliminates the need to compute the system frequency after rounding the optimal control strategy for each sample in the training set and avoids the extensive experimentation required to find suitable values of  $\zeta$ . Instead, it relies on the matrices obtained in Appendix A, the encoder, and the prediction error already computed during the training of the

encoder, thus enhancing the efficiency of  $\zeta$  design.

Here, we further discuss when does the equality holds in the inequality (28).

In the deviation of the upper bound for  $\left\| \bar{\omega}_t^{\alpha,\beta}(\bar{\mathbf{u}}_*^{\alpha,\beta}) - \omega_t^{\alpha,\beta}(Q_d(\bar{\mathbf{u}}_*^{\alpha,\beta})) \right\|$ , the first inequality in (28) and the last inequality in (29) are based on the sub-multiplicative inequality and the triangle inequality of the Frobenius norm, respectively. For any two arrays  $\mathbf{A}$  and  $\mathbf{B}$ , equality for the triangle inequality holds when the two arrays are linearly dependent, while equality for the sub-multiplicative inequality holds if and only if each row of  $\mathbf{A}$  and each column of  $\mathbf{B}$  are linearly dependent.

$\left\| \bar{\omega}_t^{\alpha,\beta}(\bar{\mathbf{u}}_*^{\alpha,\beta}) - \omega_t^{\alpha,\beta}(Q_d(\bar{\mathbf{u}}_*^{\alpha,\beta})) \right\|$  is often strictly lower than the upper bound derived in Eq.(28). The reason is the equality conditions of the triangle inequality and the sub-multiplicative inequality in (28) and (29) do not necessarily hold. The gap between  $\left\| \bar{\omega}_t^{\alpha,\beta}(\bar{\mathbf{u}}_*^{\alpha,\beta}) - \omega_t^{\alpha,\beta}(Q_d(\bar{\mathbf{u}}_*^{\alpha,\beta})) \right\|$  and its upper bound will be further illustrated in the simulation results in Section IV-E.

#### IV. CASE STUDY

In this section, the effectiveness of EKFC is illustrated by a case study on the CloudPSS platform [29], [30]. All of the following tests are conducted on PCs with Intel Xeon W-2255 processor, 3.70 GHz primary frequency, and 128GB memory.

##### A. Test System and Datasets

To validate the effectiveness of our proposed method, we conducted simulation experiments the CIGRE-LF test system, which is adapted from a real provincial power grid in China. The CIGRE-LF consists of 102 500-kV buses, and possesses a load level of 2600 MW, with installed capacities of 2400 MW and 5400 MW for renewable and conventional energy sources, respectively. The full electromagnetic transient (EMT) model of the test system is built on the CloudPSS platform [31].

The training and testing sets are generated as follows. We assume that the parameter values of inertia for each generator follow a uniform distribution, with the mean being the original manufacturer data and a deviation of 30% of the mean value to account for parameter uncertainties. We assume that  $u_i$  at bus  $i$  is a uniformly distributed random number between 0 and 1. The fault set of the system is generated by traversing N-1, N-2, and N-3 faults. The training set consists of 600 frequency trajectories, while the testing set consists of 300 frequency trajectories. Each frequency trajectory has a length of 1 min. When generating a frequency trajectory, inertia for each generator,  $u_i$ , and faults are randomly generated according to their respective distributions. Since  $u_i$  and the inertia for each generator are continuous variables, the probability of having the same  $u_i$  and inertia values for two frequency trajectories is small. Therefore, we assume that there is no intersection between the training and testing sets.

##### B. Adaptability

Fig.1 demonstrates that KLS is capable of extracting latent variables strongly correlated with the inertia rate and power

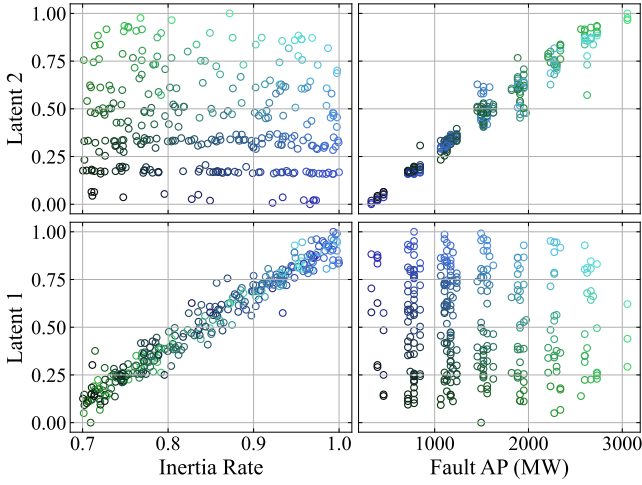


Fig. 1. The correlation between the inertia rate, power imbalance, and the outputs of the latent extractor.

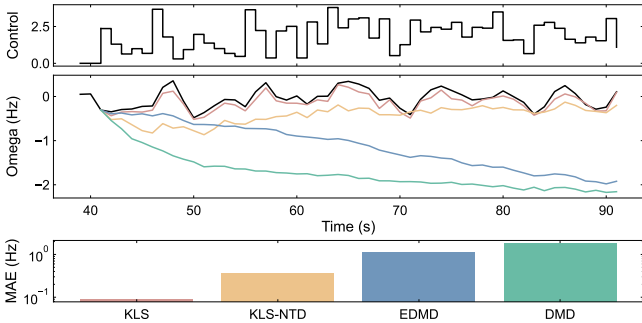


Fig. 2. Comparison between true frequency trajectory(black) and predicted frequency trajectory(pink) during future 60s with proposed KLS(pink), KLS-NTD (orange), EDMD (blue) and DMD (green). (a)Random control inputs; (b) true and predicted frequency trajectories ; (c) MAE of prediction errors.

imbalance from the frequency trajectory within a 300 ms time window after a fault occurs. Specifically, Latent1 and Latent2 exhibit a remarkably high correlation with the inertia rate and power imbalance, respectively, providing evidence that Koopman linear representations are capable of capturing parameter variations in the original state space system model using measurements. This result validates the adaptability of KLS to diverse operating conditions and faults. Furthermore, as the results presented in Fig.1 are based on the training set, it confirms that KLS is able to adapt to unanticipated operating conditions and faults.

### C. Prediction Capability

To illustrate the capability of KLS to learn the dynamics of system frequency from the online measurement, the frequency measurement of last 1 min is used to fit the linear model in Eq.(3) for the system with different inertia, control inputs and faults. As the benchmark of the learning algorithm, the DMD and EDMD method is implemented with 100 radial basis functions (RBF) as observables. KLS without time delay embedding (KLS-NTD, i.e., when  $\tau = 0$  in Eq.(4)) is also tested as a benchmark. The strong nonlinearity of dynamics makes the local linearization method hard to fit the model accurately in global horizon, and the piecewise linearization has difficulty in remaining a balance between

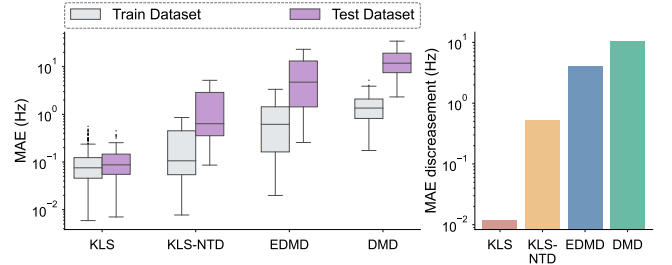


Fig. 3. Boxplot of prediction errors of different Koopman operator models.

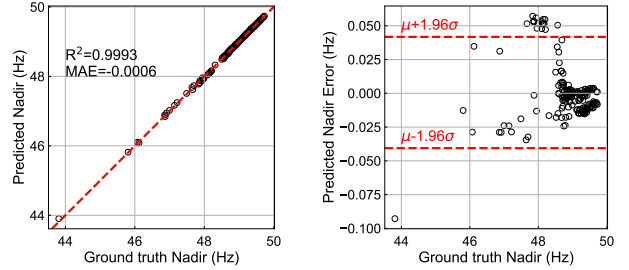


Fig. 4. Prediction accuracy of KLS for the frequency nadirs.

accuracy and simplicity. Therefore, only Koopman operator related algorithms are compared. In subsequent discussions, we refer to KLS-NTD, DMD, and EDMD as the state-of-the-art algorithms (SOTAs) for brevity and clarity.

Fig.2(b) demonstrates the global linearization capability of the proposed methods. The pink line represents the simulated dynamic process, while the blue and green lines represent the predicted results obtained from EDMD and DMD, respectively. The orange line corresponds to the predicted results obtained from KLS-NTD.

Based on the frequency sequence observed within 300ms after the generator tripping at 40s, KLS demonstrates accurate prediction of the evolving frequency for the subsequent 60 seconds under different control inputs. This highlights the effectiveness of the latent extractor combined with time-delayed measurements in capturing the dynamics of the system frequency. In contrast, DMD and EDMD exhibit poorer performance, which can be attributed to their limited capability in incorporating time-delay information and harnessing the powerful non-linear representation offered by deep learning techniques. The prediction accuracy of KLS and SOTAs on the training and testing sets is illustrated in Fig.3. The average absolute error (MAE) is employed as a measure of prediction accuracy. Due to the capability of KLS to track parameter variations in the original state space system model, the prediction accuracy is consistently high on both the training and testing sets.

For frequency control problems, the frequency nadir and steady-state value are two important indicators for assessing frequency safety. In order to demonstrate the prediction accuracy of KLS for the frequency nadir and steady-state value, we set all the inputs  $u$  in the test dataset to zero and re-simulated the true frequency trajectory. Subsequently, we computed the predicted frequency trajectory using KLS. The prediction accuracy for both indicators is shown in Fig. 4 and Fig. 5. It can be observed that the MAE of the predicted frequency trajectories for 95% of the test dataset is within

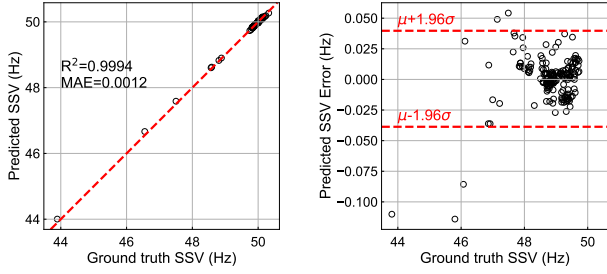


Fig. 5. Prediction accuracy of KLS for the steady-state values.

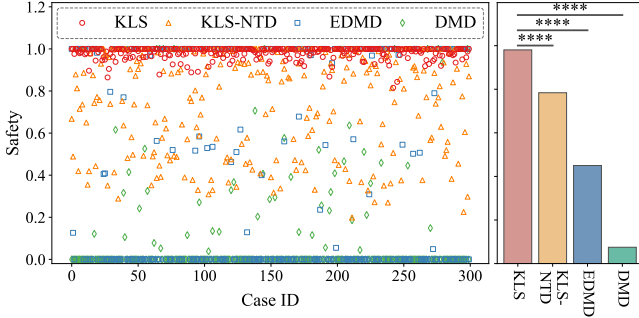


Fig. 6. The average control safety metrics of KLS, KLS-NTD, EDMD, and DMD on the test dataset.

0.1%.

#### D. Control Effect

In this subsection, we focus on investigating the impact of prediction accuracy on control effectiveness. Therefore, it is assumed that a continuous adjustment of load shedding can be achieved, and the safety margin  $\zeta$  is set to zero. The effectiveness of KLS and SOTAs is evaluated by assessing the system's frequency safety after the implementation of these control strategies. Furthermore, to demonstrate the adaptability of KLS to unanticipated operating conditions and faults, all results in this subsection are computed using the test dataset. The normalized safety metric is calculated as follows:

$$Safety = \alpha \left( \frac{Nadir^* - Nadir_0}{Nadir_1 - Nadir_0} \right) + \beta \left( \frac{SSV^* - SSV_0}{SSV_1 - SSV_0} \right) \quad (31)$$

In Eq.(31), when the frequency nadir is greater than  $Nadir_1$  and the steady-state frequency is greater than  $SSV_1$ ,  $Safety$  is assigned a value of 1; when the system's frequency nadir  $Nadir^*$  is less than  $Nadir_0$  and the steady-state frequency  $SSV^*$  is less than  $SSV_0$ ,  $Safety$  is assigned a value of 0. The weights for measuring the safety indicators of nadir and steady-state value are represented by  $\alpha$  and  $\beta$ , respectively. In this paper, the values of  $Nadir_1$  and  $SSV_1$  are set to 49.0Hz and 49.5Hz, respectively, which are equal to  $\omega_{\min}$  and  $\omega_{\infty \min}$ .  $Nadir_0$  and  $SSV_0$ , and  $SSV_1$  are set to 48.5Hz and 49.0Hz, respectively. The values of  $\alpha$  and  $\beta$  are both set to 0.5. The average control safety metrics of KLS, KLS-NTD, EDMD, and DMD on the test dataset are depicted in Fig.6. Among the 300 test data, the proportions of  $Safety$  exceeding 0.9 for these methods are 97.5%, 49.3%, 41.6%, and 4% respectively. KLS, with its superior predictive accuracy compared to SOTAs, enhances the system's frequency safety.

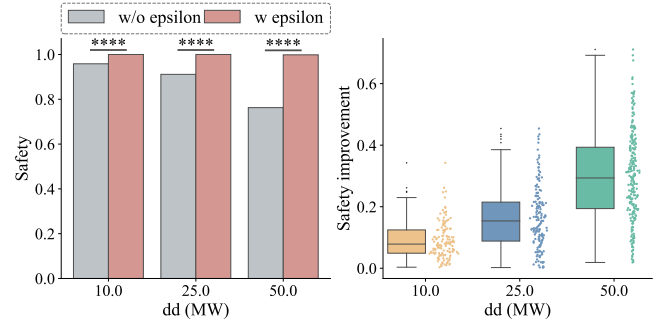


Fig. 7. The improvement in Safety when incorporating the safety margin.

However, without incorporating a safety margin into the frequency constraints of the optimal control problem Eq. (5), the average control safety metric of KLS fails to reach a value of 1. In Fig.4 and Fig.5, approximately 2.5% of the test data exhibit prediction errors exceeding +0.05Hz. Furthermore, KLS tends to overestimate the frequency nadir and steady-state frequency for these 2.5% of the test data, resulting in relatively conservative control measures. As a result, around 2.5% of the post-control frequency trajectories fall below the safety metric threshold of 0.9. Considering the feasible load shedding amounts and the discrepancy from the optimal control obtained through Eq.(5), further deterioration of KLS's  $Safety$  would occur. This observation underscores the necessity of incorporating a safety margin in the frequency constraints of the optimal control problem.

#### E. Safety Margin

This subsection analyzes the control effectiveness after the introduction of a safety margin in Subsection III-B. The evaluation of control measures is based on two indicators: the system's frequency safety and the control cost. Increasing the amount of load shedding typically results in a higher system frequency. If the system frequency remains within the safe range (i.e., safety = 1), the greater the deviation of the nadir and the steady-state value of the system's frequency from the specified hard limits, the higher the associated control cost becomes. To tackle this issue, a normalized economic metric, ranging from 0 to 1, is introduced as an indicator to measure the control cost.

$$economy = \min \left( \frac{Nadir^* - Nadir_0}{Nadir_1 - Nadir_0}, \frac{SSV^* - SSV_0}{SSV_1 - SSV_0} \right) \quad (32)$$

where  $Nadir_1 = -1$  and  $SSV_1 = -0.5$  indicate that when the nadir is equal to -1 and the steady-state value is equal to -0.5, the economic efficiency of load shedding measures is assigned a value of 1. Similarly,  $Nadir_0 = -0.5$  and  $SSV_0 = 0$  indicate that when the nadir is greater than -0.5 and the steady-state value is greater than 0, the economic efficiency of load shedding measures is assigned a value of 0.

Fig. 7 presents the improvement in  $Safety$  when incorporating the safety margin calculated using Eq.(5) at different values of  $d$  (where  $d$  takes values of 10MW, 25MW, and 50MW). It can be observed that the introduction of the safety margin enhances the system's frequency safety for different

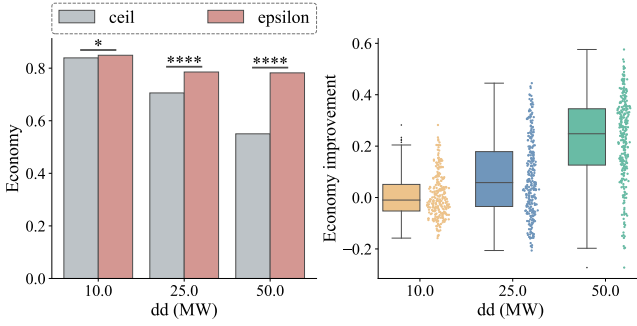


Fig. 8. The economic efficiency of KLS-C and KLS.

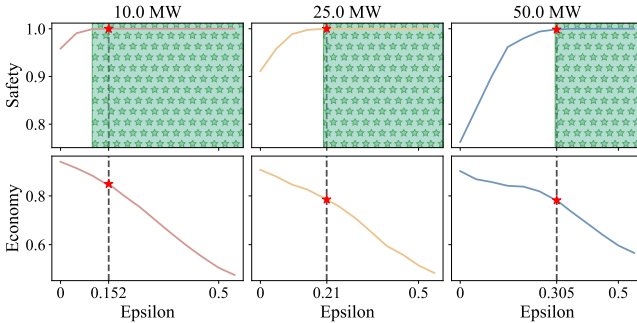


Fig. 9. Comparison between the ideal safety margin and the safety margin calculated by Eq.(30).

load levels associated with a feeder. Moreover, as  $d$  increases, the improvement in *Safety* becomes more significant.

For the sake of clarity, we will refer to the control strategy derived by assigning the optimal solution of Eq. (5) to a feasible load shedding value based on Eq. (7) as the ceiled KLS (KLS-C). The economic efficiency of KLS-C and KLS is demonstrated in Fig. 8. It can be observed that by avoiding the rounding of the optimal load shedding amount to the nearest larger value, KLS achieves a reduced amount of load shedding while ensuring the safety of the system frequency.

Fig. 9 presents the safety margin calculated in Eq. (25). Firstly, under different values of  $d$  (10MW, 25MW, and 50MW), we simulated the *Safety* and *Economy* index of KLS for various values of  $\zeta$  ranging from 0 to 0.5. In Fig. 9, the green region represents the system satisfying  $Safety = 1$ . The boundary between the green and white regions corresponds to an  $\zeta$  that ensures system safety, while reaching a minimum load shedding amount. Next, under different values of  $d$  (10MW, 25MW, and 50MW),  $\zeta$  was calculated using Eq. (25). The calculated values of  $\zeta$  obtained from Eq. (25) are 0.152, 0.21, and 0.305, respectively. It can be observed that the  $\zeta$ s computed by the right hand side in (25) are slightly larger than the ideal values obtained by iterating over different  $\zeta$  values. This discrepancy arises from the difficulty in satisfying the inequality in Eq. (25). However, the  $\zeta$ s obtained by Eq. (25) ensure the system's frequency safety.

## V. CONCLUSION

In this paper, a novel data-enabled predictive control algorithm KLS, which adapts to diverse operating conditions and under frequency events, is introduced to achieve the optimal one-shot load shedding for power system frequency safety. To address approximation inaccuracies and the restriction of load

shedding to discrete values, a safety margin tuning scheme is incorporated within the framework of KLS. Simulation results demonstrate that KLS effectively captures latent variables strongly correlated with the inertia rate and power imbalance within a 300 ms time window after a fault occurs. The algorithm exhibits high prediction accuracy on both the training and testing sets, indicating its generalizability beyond the training set. Furthermore, the proposed safety margin tuning scheme enhances the system's frequency safety.

## REFERENCES

- [1] C. Li, Y. Wu, Y. Sun, H. Zhang, Y. Liu, Y. Liu, and V. Terzija, "Continuous under-frequency load shedding scheme for power system adaptive frequency control," *IEEE Transactions on Power Systems*, vol. 35, no. 2, pp. 950–961, 2020.
- [2] T. Amraee, M. G. Dabagh, A. Soroudi, and A. Keane, "Probabilistic under frequency load shedding considering rocof relays of distributed generators," *IEEE Transactions on Power Systems*, vol. 33, no. 4, pp. 3587–3598, 2018.
- [3] F. Ceja-Gomez, S. S. Qadri, and F. D. Galiana, "Under-frequency load shedding via integer programming," *IEEE Transactions on Power Systems*, vol. 27, no. 3, pp. 1387–1394, 2012.
- [4] S. S. Banijamali and T. Amraee, "Semi-adaptive setting of under frequency load shedding relays considering credible generation outage scenarios," *IEEE Transactions on Power Delivery*, vol. 34, no. 3, pp. 1098–1108, 2019.
- [5] X. Shiyun, W. Ping, Z. Bing, Y. J., and C. Z., "Coordinated control strategy of interconnected grid integrated with uhvdc transmission line from hami to zhengzhou," *Power Syst. Technol.*, vol. 39, no. 7, p. 6, 2015.
- [6] X. Chen, G. Qu, Y. Tang, S. Low, and N. Li, "Reinforcement learning for selective key applications in power systems: Recent advances and future challenges," *IEEE Transactions on Smart Grid*, vol. 13, no. 4, pp. 2935–2958, 2022.
- [7] H. Golpîra, H. Bevrani, A. Román Messina, and B. Francois, "A data-driven under frequency load shedding scheme in power systems," *IEEE Transactions on Power Systems*, vol. 38, no. 2, pp. 1138–1150, 2023.
- [8] Q. Shi, F. Li, and H. Cui, "Analytical method to aggregate multi-machine sfr model with applications in power system dynamic studies," *IEEE Transactions on Power Systems*, vol. 33, no. 6, pp. 6355–6367, 2018.
- [9] Z.-S. Hou and Z. Wang, "From model-based control to data-driven control: Survey, classification and perspective," *Information Sciences*, vol. 235, pp. 3–35, 2013, data-based Control, Decision, Scheduling and Fault Diagnostics. [Online]. Available: <https://www.sciencedirect.com/science/article/pii/S0020025512004781>
- [10] M. Korda, Y. Susuki, and I. Mezić, "Power grid transient stabilization using koopman model predictive control," *IFAC-PapersOnLine*, vol. 51, no. 28, pp. 297–302, 2018, 10th IFAC Symposium on Control of Power and Energy Systems CPES 2018. [Online]. Available: <https://www.sciencedirect.com/science/article/pii/S2405896318334372>
- [11] K. Champion, B. Lusch, J. N. Kutz, and S. L. Brunton, "Data-driven discovery of coordinates and governing equations," *Proceedings of the National Academy of Sciences*, vol. 116, no. 45, pp. 22445–22451, 2019. [Online]. Available: <https://www.pnas.org/doi/abs/10.1073/pnas.1906995116>
- [12] J. Xie and W. Sun, "Distributional deep reinforcement learning-based emergency frequency control," *IEEE Transactions on Power Systems*, vol. 37, no. 4, pp. 2720–2730, 2022.
- [13] W. Cui, Y. Jiang, and B. Zhang, "Reinforcement learning for optimal primary frequency control: A lyapunov approach," *IEEE Transactions on Power Systems*, vol. 38, no. 2, pp. 1676–1688, 2023.
- [14] S. L. Brunton, M. Budišić, E. Kaiser, and J. N. Kutz, "Modern koopman theory for dynamical systems," *SIAM Review*, vol. 64, no. 2, pp. 229–340, 2022. [Online]. Available: <https://doi.org/10.1137/21M1401243>
- [15] E. Kaiser, J. N. Kutz, and S. L. Brunton, "Data-driven discovery of koopman eigenfunctions for control," *Machine Learning: Science and Technology*, vol. 2, no. 3, p. 035023, jun 2021. [Online]. Available: <https://doi.org/10.1088/2632-2153/abf0f5>
- [16] Q. Cao, C. Shen, and Y. Liu, "Data-driven emergency frequency control for multi-infeed hybrid ac-dc system," *IEEE Transactions on Power Systems*, pp. 1–13, 2023.
- [17] C. Shen, Q. Cao, M. Jia, Y. Chen, and S. Huang, "Concepts, characteristics and prospects of application of digital twin in power system," *Proceedings of the CSEE*, vol. 42, no. 2, p. 487–498, 2022.

- [18] A. A. Zadeh, A. Sheikhi, and W. Sun, "A novel probabilistic method for under frequency load shedding setting considering wind turbine response," *IEEE Transactions on Power Delivery*, vol. 37, no. 4, pp. 2640–2649, 2022.
- [19] D. Q. Mayne, "Model predictive control: Recent developments and future promise," *Automatica*, vol. 50, no. 12, pp. 2967–2986, 2014. [Online]. Available: <https://www.sciencedirect.com/science/article/pii/S0005109814005160>
- [20] Y.-Y. Hong and C.-Y. Hsiao, "Under-frequency load shedding in a standalone power system with wind-turbine generators using fuzzy pso," *IEEE Transactions on Power Delivery*, vol. 37, no. 2, pp. 1140–1150, 2022.
- [21] S. ichi Azuma and T. Sugie, "Optimal dynamic quantizers for discrete-valued input control," *Automatica*, vol. 44, no. 2, pp. 396–406, 2008. [Online]. Available: <https://www.sciencedirect.com/science/article/pii/S0005109807003068>
- [22] R. Larson, "Optimum quantization in dynamic systems," *IEEE Transactions on Automatic Control*, vol. 12, no. 2, pp. 162–168, 1967.
- [23] B. O. Koopman, "Hamiltonian systems and transformation in hilbert space," *Proceedings of the National Academy of Sciences*, vol. 17, no. 5, pp. 315–318, 1931.
- [24] Y. Xu, M. Netto, and L. Mili, "Propagating parameter uncertainty in power system nonlinear dynamic simulations using a koopman operator-based surrogate model," *IEEE Transactions on Power Systems*, vol. 37, no. 4, pp. 3157–3160, 2022.
- [25] F. Takens, "Detecting strange attractors in turbulence," *Lecture Notes in Mathematics*, p. 366–381, 1981.
- [26] M. Korda and I. Mezić, "Linear predictors for nonlinear dynamical systems: Koopman operator meets model predictive control," *Automatica*, vol. 93, pp. 149–160, 2018. [Online]. Available: <https://www.sciencedirect.com/science/article/pii/S000510981830133X>
- [27] S. Chen, H. Wang, M. Morari, V. M. Preciado, and N. Matni, "Robust closed-loop model predictive control via system level synthesis," 2019.
- [28] J. Anderson, J. C. Doyle, S. H. Low, and N. Matni, "System level synthesis," *Annual Reviews in Control*, vol. 47, pp. 364–393, 2019. [Online]. Available: <https://www.sciencedirect.com/science/article/pii/S1367578819300215>
- [29] Y. Song, Y. Chen, Z. Yu, S. Huang, and C. Shen, "Cloudpss: A high-performance power system simulator based on cloud computing," *Energy Reports*, vol. 6, pp. 1611–1618, 2020, 2020 The 7th International Conference on Power and Energy Systems Engineering. [Online]. Available: <https://www.sciencedirect.com/science/article/pii/S2352484720317297>
- [30] "MS Windows NT kernel description," <https://www.cloudpss.net/>, accessed: 2022-06-24.
- [31] Y. Liu, Y. Song, Z. Yu, C. Shen, and Y. Chen, "Modeling and simulation of hybrid ac-dc system on a cloud computing based simulation platform - cloudpss," in *2018 2nd IEEE Conference on Energy Internet and Energy System Integration (EI2)*, 2018, pp. 1–6.

## B. Loss function

$$\mathcal{L} = \sum_{t=1}^T \|\hat{g}_t - g_t\| \quad (33)$$

The loss function used in training is a weighted sum of four terms: autoencoder reconstruction  $L_{recon}$ , SINDy prediction on the input variables  $L_{dx/dt}$ , SINDy prediction on the encoder variables  $L_{dz/dt}$ , and SINDy coefficient regularization  $L_{reg}$ . For a data set with  $m$  input samples, each loss is explicitly defined as follows:

## APPENDIX A

### NETWORK ARCHITECTURE AND TRAINING

#### A. Network architecture

The network architecture is depicted in Fig ???. The network consists of three types of modules: ResConv block, Temporal Average, and Fully Connected. The ResConv block utilizes convolutional layers to learn and identify specific temporal patterns or trends in the time series data. The inclusion of residual connections plays a vital role in enabling the stacking of multiple convolutional layers to effectively extract parameter variations in a state-space model from the time series data. The Temporal Average and Fully Connected modules are responsible for weighted averaging of time series features and feature extraction, respectively. The ResConv block comprises three convolutional layers with kernel sizes of 5, 3, and 3, respectively. A residual connection is incorporated by using a convolutional layer followed by a batch normalization layer. The Fully Connected module consists of three fully connected networks, employing ReLU activation functions.